AGU PUBLICATIONS

Geophysical Research Letters

RESEARCH LETTER
10.1002/2014GL061216

Key Points:
- Ice cloud and snow surface radiative properties vary considerably in the far IR
- Snow surface emissivity and cloud scattering affect far IR comparably
- Even for far-IR radiation alone, the impact is nonnegligible

Supporting Information:
- Text S1
- Figure S1
- Figure S2
- Figure S3
- Table S1

Correspondence to:
X. Huang,
xianglei@umich.edu

Citation:
Chen, X., X. Huang, and M. G. Flanner (2014), Sensitivity of modeled far-IR radiation budgets in polar continents to treatments of snow surface and ice cloud radiative properties, *Geophys. Res. Lett.*, *41*, 6530–6537, doi:10.1002/2014GL061216.

Received 14 JUL 2014
Accepted 4 SEP 2014
Accepted article online 5 SEP 2014
Published online 24 SEP 2014

Sensitivity of modeled far-IR radiation budgets in polar continents to treatments of snow surface and ice cloud radiative properties

Xiuhong Chen[1], Xianglei Huang[1], and Mark G. Flanner[1]

[1]Department of Atmospheric, Oceanic, and Space Sciences, University of Michigan, Ann Arbor, Michigan, USA

Abstract While most general circulation models assume spectrally independent surface emissivity and nonscattering clouds in their longwave radiation treatment, spectral variation of the index of refraction of ice indicates that in the far IR, snow surface emissivity can vary considerably and ice clouds can cause nonnegligible scattering. These effects are more important for high-elevation polar continents where the dry and cold atmosphere is not opaque in the far IR. We carry out sensitivity studies to show that in a winter month over the Antarctic Plateau including snow surface spectral emissivity and ice cloud scattering in radiative transfer calculation reduces net upward far-IR flux at both top of atmosphere and surface. The magnitudes of such reductions in monthly mean all-sky far-IR flux range from 0.72 to 1.47 Wm^{-2}, with comparable contributions from the cloud scattering and the surface spectral emissivity. The reduction is also sensitive to sizes of both snow grains and cloud particles.

1. Introduction and Motivation

Understanding the response of polar climate to global warming is one of the key challenges to be addressed in the study of climate change [e.g., *Anisimov et al*., 2007]. General circulation models (GCMs) have been used extensively in studying this question [e.g., *Holland and Bitz*, 2003; *Shindell*, 2007; *Armour et al*., 2011; *Screen et al*., 2012; *Kay et al*., 2012]. Longwave radiation plays an important role in the polar energy budget and climate. The far-IR portion (0–600 cm^{-1}) of the longwave spectrum contributes ~50% of the outgoing longwave radiation, and water vapor pure rotational bands dominate atmospheric absorption and emission in the far IR [*Harries et al*., 2008]. Under most circumstances, the water vapor in the atmosphere is abundant enough to render the atmosphere opaque in the far IR. In these circumstances the surface far-IR emission is completely absorbed within the troposphere and does not reach the top of atmosphere (TOA). However, this scenario is not applicable to polar continents, especially high-elevation areas such as the Antarctic Plateau and Greenland, where the temperatures are cold and, due to high altitude, the total column water vapor (CWV) is much smaller than that in other places. For example, the global mean CWV is ~2.2 cm but the CWV above Antarctica is only 0.1–0.3 cm [*Ye et al*., 2007]. The CWV above Greenland in the wintertime is also well below 0.5 cm [*Neely and Thayer*, 2011]. Moreover, the low surface pressure in these areas results in less pressure broadening of absorption lines. These facts all help reduce the overall atmospheric absorption of far-IR radiation in polar environments, enabling surface far-IR emission to reach the TOA. Figures 1a and 1b show annual mean change of the TOA outgoing far-IR flux due to a 1 K perturbation of surface temperature, for both clear-sky and all-sky conditions, which are computed using an off-line spectrally resolved radiative transfer model [*Chen et al*., 2013]. The change in outgoing far-IR flux is only significant over polar high-elevation areas, the Tibetan Plateau, and the Andes Mountain. For the Antarctic Plateau and Greenland, 1 K surface temperature changes result in ~0.6 Wm^{-2} change in clear-sky and ~0.3 Wm^{-2} change in all-sky outgoing far IR, respectively.

As far as we are aware of, most state-of-the-art GCMs assume spectrally independent surface emissivity in their longwave radiation scheme, and usually, the emissivity is assumed to be unity. Except a few GCMs such as Canadian CanAM4 [*Li*, 2002; *von Salzen et al*., 2013], most GCMs also assume nonscattering clouds in their longwave radiation scheme. We use longwave rapid radiative transfer model (RRTM_LW) [*Mlawer et al*., 1997; *Iacono et al*., 2000] with ice cloud parameterization from *Fu et al*. [1998] to investigate the impact of inclusion of LW scattering for two typical sounding profiles of midlatitude winter and subarctic winter [*McClatchey et al*., 1972] with varying total column water vapor. The surface is assumed to be blackbody for

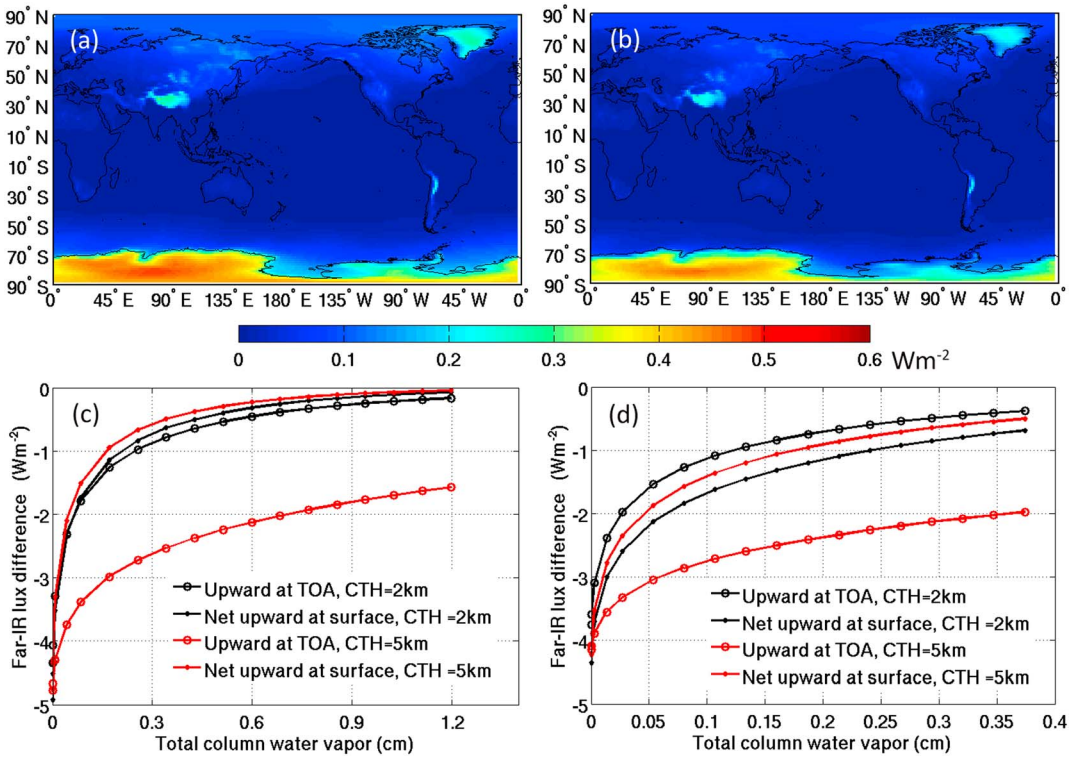

Figure 1. (a) The annual mean change of TOA far-IR clear-sky flux (0–600 cm^{-1}) due to 1 K increase in surface temperature. (b) Same as Figure 1a except for the change of TOA far-IR all-sky flux. The 1 K surface temperature perturbation is applied to 6-hourly output of ECMWF ERA-Interim reanalysis data in 2002 [*Dee et al.*, 2011]. (c) The far-IR flux difference at both the TOA and the surface caused by scattering of clouds while everything else remains the same. The difference is shown as a function of total column water vapor. Cloud visible optical depth is assumed to be 0.5, and effective size is 25 μm. Midlatitude winter sounding profiles from *McClatchey et al.* [1972] are used here, and a constant is used to scale the entire humidity profile. CTH on the plot denotes cloud top height. (d) Same as Figure 1c but using subarctic winter sounding profiles from *McClatchey et al.* [1972].

this calculation. RRTM_LW has three bands in the far IR from 0 to 630 cm^{-1}. The built-in eight-stream discrete ordinates radiative transfer (DISORT) solver [*Stamnes et al.*, 1988] is used for multiple scattering calculations. RRTM_LW has been extensively benchmarked against line-by-line radiative transfer models [*Mlawer et al.*, 1997; *Clough et al.*, 2005]. Results found here using eight-stream and 16-stream DISORT solvers were within 0.01% of each other. As shown in Figures 1c and 1d, inclusion of cloud scattering reduces the TOA upward flux because part of the upward flux incident on the cloud is now scattered in other directions instead of going through and reaching the TOA, and this dominates over other changes due to scattering. It also reduces the net upward far-IR flux at surface because of the backward scattering of the upward flux. The magnitude of such changes monotonically decreases with increasing CWV. When CWV is more than 0.8 cm, all changes are close to zero except the change of TOA upward flux when high clouds are present. Results from Figures 1c and 1d are consistent with previous studies on the effect of cloud LW scattering by *Chou et al.* [1999] and *Costa and Shine* [2006], which studied the overall impacts on the LW broadband fluxes instead of the far IR alone.

While neither atmospheric scattering nor surface reflection exists in the longwave treatments of most current GCMs (Figure 2a), in reality the surface emissivity is spectrally dependent and clouds can scatter longwave radiation as well (Figure 2b). For high-elevation polar continents, the issues of surface emissivity and cloud longwave scattering become coupled in the far IR. As described above, there is less water vapor in polar atmospheres to absorb far-IR radiation than elsewhere. Thus, part of the surface far-IR emission can reach the cloud, and if both surface and cloud can scatter far-IR photons, multiple reflections can happen between cloud and surface (in addition to multiple scattering in the clouds), indicating important coupling between the treatments of spectral snow emissivity and cloud scattering. As a matter of fact, m_{ice}, the imaginary part of the index of refraction of ice (Figure 2c) has a local minimum between 350 and 550 cm^{-1}, implying that the

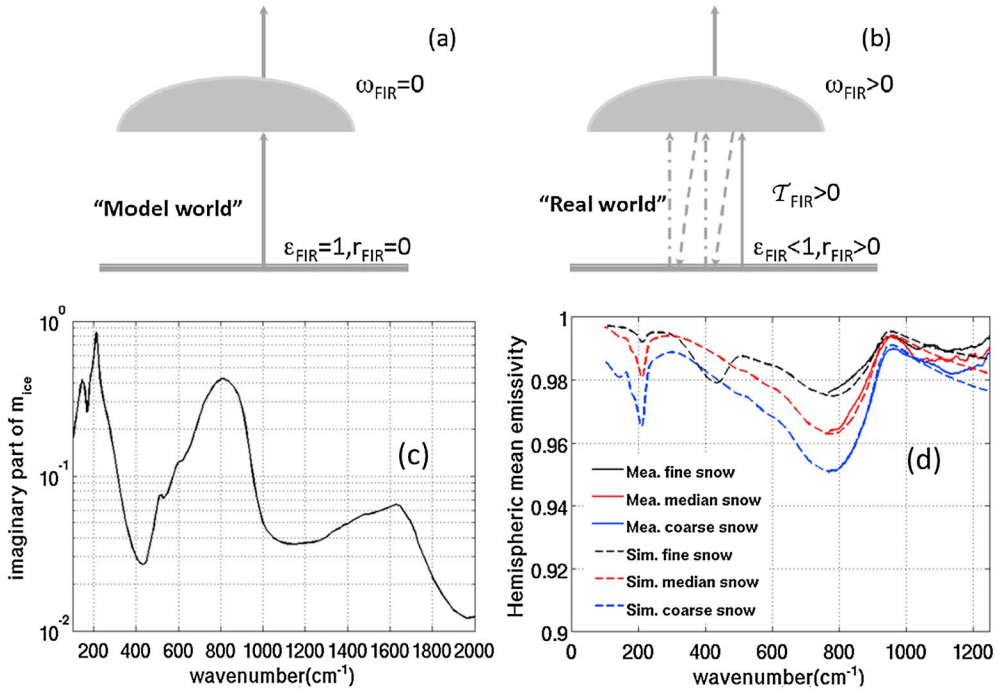

Figure 2. (a) A schematic showing the current assumptions used in most GCMs for the relevant optical properties of surface and cloud in the far IR (denoted by subscript "FIR"). Upward arrow denotes the upward far-IR flux emitted by the surface and transmitted through the cloud. $\mathcal{T}$ is transmittance, ω is the single-scattering albedo of cloud, ε is the surface emissivity, and r is the surface reflectivity. No scattering happens in the far IR in "model world." (b) A schematic showing the real radiation interactions between clouds and snow surface. Photons in the far IR can be reflected between cloud and surface multiple times and absorbed in the course of such scattering. (c) The imaginary part of the index of refraction of ice from 100 to 2000 cm^{-1}. (d) Comparison of simulated and measured hemispherical mean snow emissivity for fine, medium, and coarse snows. Measured results are shown in solid lines. Simulated results are shown in dash-dotted lines. Fine, medium, and coarse snows are in black, red, and blue lines, respectively.

scattering effects of ice clouds and snow or ice surfaces are more prominent over this spectral range than over the middle IR.

The facts mentioned above motivate us to examine how the treatments outlined in Figures 2a and 2b can affect the longwave radiation budget at both the TOA and surface of high-elevation polar continents. In reality, great complexity exists in the spectral emissivity of snow at different aging stages and in the microphysical and optical properties of polar clouds. This study is not aimed at providing the most accurate estimation of the far-IR energy budget for the polar region. Instead, we carried out sensitivity studies with reanalysis and observation-based parameters to assess the magnitude of changes in simulated far-IR radiation budgets when surface spectral emissivity and cloud scattering are more realistically treated. In section 2 we discuss the calculation of far-IR spectral emissivity of snow surfaces. Sensitivity studies are presented in section 3. Conclusions and further discussion are given in section 4.

2. The Far-IR Spectral Emissivity of Snow Surface

While there have been extensive measurements of surface spectral emissivity for a variety of surface types, such as the Spectral Library for the Advanced Spaceborne Thermal Emission and Reflection Radiometer [*Baldridge et al.*, 2009], such measurements only cover the middle IR (>650 cm^{-1}). There have been no compilations of far-IR spectral emissivity of different surface types nor any systematic measurements of far-IR emissivity of snow or ice surfaces. The spectral emissivity of snow surfaces can, in principle, be modeled with certain assumptions [e.g., *Berger*, 1979; *Wiscombe and Warren*, 1980; *Warren*, 1982]. Given the lack of actual measurements, we rely on such modeling approaches in this study.

The refractive indices of ice from *Warren and Brandt* [2008] are used in our modeling of snow spectral emissivity. The snow grain size distribution is assumed to be lognormal. *Wald* [1994] pointed out that the

Table 1. The Far-IR Flux Integrated From 0 to 630 cm^{-1} (in Wm^{-2}) at the TOA and Surface as Well as Atmospheric Net Emission for Different Treatments of Ice Cloud and Surface Emissivity in the Far IR[a]

		Treatment 1 (Wm^{-2})	Difference From Treatment 1 (Wm^{-2})		
	Cloud Effective Size	Case 0: Blackbody Surface and Nonscattering Clouds	Case 1: Fine Snow Surface and Scattering Clouds	Case 2: Coarse Snow Surface and Scattering Clouds	Case 3: Blackbody Surface and Scattering Clouds
Far-IR upward	25 μm	80.40	−1.31	−1.47	−1.00
flux at TOA	50 μm	80.70	−0.84	−1.0	−0.51
Far-IR upward	25 μm	82.97	−0.37	−0.53	0
flux at surface	50 μm	82.97	−0.39	−0.56	0.0
Far-IR downward	25 μm	59.37	0.65	0.65	0.66
flux at surface	50 μm	58.24	0.33	0.33	0.33
Far-IR net upward	25 μm	23.60	−1.02	−1.17	-0.66
flux at surface	50 μm	24.73	−0.72	−0.89	-0.33
Net atmospheric	25 μm	56.80	−0.29	−0.29	−0.35
far-IR emission	50 μm	55.97	−0.12	−0.12	−0.18

[a]Satellite observations of cloud profiles and ERA-Interim reanalysis in July 2008 over Antarctic Plateau (surface elevation >2 km) are fed into RRTM_LW to derive these results.

single-scattering albedo and the asymmetry parameter computed by Mie theory cannot be directly used in radiative transfer models of closely packed grains. *Mishchenko* [1994] and *Mishchenko and Macke* [1997] proposed a method named "static structure factor correction," which is based on solving Maxwell's equations and statistical mechanics for dense packing. The method modifies optical properties derived from the Mie scattering theory with a static structure factor. Details of the method can be found in *Mishchenko* [1994]. This correction method can be used for particles of any grain size and thus is adopted in this study. The corrected single-scattering parameters are then fed into the Hapke emissivity model [*Hapke*, 1993] to simulate snow emissivity at all spectral frequencies in the longwave. This method uses snow effective grain size as an input parameter; it thus holds promise for incorporation into models like the Community Earth System Model, which currently prognoses vertically resolved snow effective radius [e.g., *Oleson et al*., 2010].

Figure 2d shows the comparison between modeled and measurement-based hemispherical mean snow spectral emissivities for fine-, medium-, and coarse-grained snow surfaces as defined in *Hori et al*. [2006]. For coarse snow, the rough surface welding effect [*Wald*, 1994] needs to be considered and Fresnel reflective model [*Masuda et al*., 1988] is used to model this effect. As a result, the spectral emissivity for coarse snow is computed by a weighted average of the emissivity from the Hapke model (weighting factor 0.97) and the Fresnel reflective model (weighting factor 0.03). The weighting factors are determined for the best match with measured coarse snow spectral emissivity. Solid lines are based on directional snow emissivity at six viewing zenith angles from 0° to 75° with an increment of 15° measured by *Hori et al*. [2006] in the spectral range of 714–1250 cm^{-1}. The diameter ranges of fine, medium, and coarse snows are 40–100 μm, 300–1100 μm, and 50–1000 μm, with median diameters of 70 μm, 600 μm, and 800 μm, respectively. Detailed information of snow types can be found in Table 1 of *Hori et al*. [2006]. Figure S1 in the supporting information shows the comparison of simulated and measured directional snow emissivity at three viewing zenith angles (15°, 45°, and 75°) for the case of coarse snow. Figures 2d and S1 show that our modeled snow spectral emissivity agrees reasonably well with measurements, including dependencies on both grain size and viewing angle. This gives us confidence in using the modeled far-IR emissivity in this study. Figure 2d also shows that, in general, the larger the snow grain size is, the lower the spectral emissivity, which is in agreement with *Wald* [1994].

3. Sensitivity Studies of the Impact on Surface and TOA Energy Budget

Using the spectral emissivities modeled in section 2, we carry out two sensitivity studies. The area of interest is the Antarctic Plateau between 70°S and 82°S with surface altitude above 2 km (satellite data used in this section are only available as far south as 82°S). As in Figure 1, RRTM_LW is used with the ice cloud parameterization from *Fu et al*. [1998]. Therefore, for the following discussion, the far-IR flux refers to the flux integrated from 0 to 630 cm^{-1}. For a cirrus cloud with effective size of 25 μm, the ratio of far-IR optical depth to its visible optical depth at 0.55 μm is ~1.12.

For the first sensitivity study, we randomly pick a month in austral winter, i.e., July 2008 and use the European Centre for Medium-Range Weather Forecasts (ECMWF) ERA-Interim reanalysis [*Dee et al*., 2011] monthly mean temperature and humidity profiles over the aforementioned Antarctic region as input to RRTM_LW. The results are similar when data of another month in austral winter are used. If clear sky is assumed, the difference between fine snow surface emissivity and blackbody surface causes -0.37 Wm^{-2} change (i.e., -0.45% in percentage change) in the TOA upward far-IR flux and -0.41 Wm^{-2} (-1.63%) change in the surface net upward far-IR flux. If coarse snow is assumed, the corresponding changes are -0.54 Wm^{-2} (-0.67%) at the TOA and -0.59 Wm^{-2} (-2.33%) at the surface.

Next, we assume a 1 km layer of ice cloud specified with different optical depths and cloud top heights in the RRTM_LW calculation. We compute the far-IR flux at both TOA and surface using two treatments: Treatment 1 is similar to assumptions used in most current GCMs—blackbody surface and nonscattering ice cloud (Figure 2a) and Treatment 2 takes spectrally varying surface emissivity and scattering ice cloud into account (Figure 2b). We compute the net upward far-IR flux differences at both the TOA and surface between the two treatments for different combinations of cloud top height and cloud optical depth, summarized in Figure 3. As shown in Figures 1c and 1d, inclusion of cloud LW scattering reduces the upward flux at the TOA and increases the downward flux at the surface (i.e., reduces the net upward flux at surface). Employing spectrally varying surface emissivity instead of blackbody emissivity also reduces upward flux at surface. The far-IR flux change at the TOA (Figures 3a and 3b) has little sensitivity to the surface spectral emissivity but depends on both cloud top height and cloud optical depth. As for the net upward flux at the surface, the change is much more sensitive to the cloud optical depth than to the cloud top height, with largest change occurring with cloud optical depths of ~1–2. Comparing the clear-sky results mentioned in the previous paragraph, the all-sky net upward far-IR flux changes at both TOA and surface, as shown in Figure 3, are severalfold larger. Comparing Figures 3c and 3d, the difference due to surface emissivities of fine and coarse snow is ~0.1–0.2 Wm^{-2}. Figures 3e and 3f show the difference in atmospheric net far-IR emission (i.e., TOA upward flux-surface net upward flux). When cloud top is low ($<$2.5 km) and cloud visible optical depth is no more than 1 (for 2.5 km cloud top) or 3 (for 1.5 km cloud top), the difference is positive, implying that inclusion of scattering increases the net far-IR emission by the atmosphere. For the other cases, the difference is negative and the LW cloud scattering leads to more atmospheric net absorption of far-IR flux than the LW cloud absorption alone.

It is well known that the cirrus optical properties can change significantly with their effective particle size. To investigate the sensitivity, we compute the far-IR flux difference between Treatment 2 and Treatment 1 for one case of low cloud (cloud top at 2 km) and one case of high cloud (cloud top at 5 km) with varying effective size of cirrus particle. Figure 4 summarizes the results and shows that the difference in both TOA and surface net upward far-IR flux decreases with the increases of cloud effective particle size. When cloud effective particle size increases from 15 μm to 80 μm, the differences reduce by ~55%–60% for both high cloud and low cloud, for both TOA and net surface upward flux in the far IR, and for both fine and coarse snow surfaces.

The second sensitivity study utilizes actual retrievals of cloud profiles based on CloudSat and CALIPSO observations. By doing so, we take realistic cloud occurrences into account. We use all CloudSat and CALIPSO observations from July 2008 over the same Antarctic region with surface elevation above 2 km. The ERA-Interim 6-hourly temperature and humidity reanalyses are interpolated to the same location and time as the satellite observations. Cloud liquid water content profiles are from CloudSat product 2B-CWC-RVOD [*Wood*, 2008]. Cloud ice water content profiles are from a joint retrieval using both CALIPSO lidar and CloudSat radar observations, which is released as a CloudSat Level 2 data product and commonly referred to as 2C-ICE [*Deng et al*., 2010]. In total, 624,275 observations are available and 46% of them are clear-sky observations. Geographical locations of these profiles have nearly uniform coverage over the Antarctic Plateau above 2 km elevation (Figure S2 in the supporting information). The far-IR flux at both TOA and surface, as well as the atmospheric net far-IR emission (i.e., TOA outgoing flux-surface net upward flux), are averaged over all profiles and summarized in Table 1. To make the comparisons informative, we also list the results assuming a blackbody surface and scattering cloud (Case 3 in Table 1). *Walden et al*. [2003] analyzed precipitating ice crystals collected at South Pole Station of Antarctica during the winter of 1992 and found that most of the crystals have effective radius of ~11 μm (i.e., effective size of ~22 μm). Thus, we compute two scenarios assuming 25 μm and 50 μm cirrus effective particle sizes.

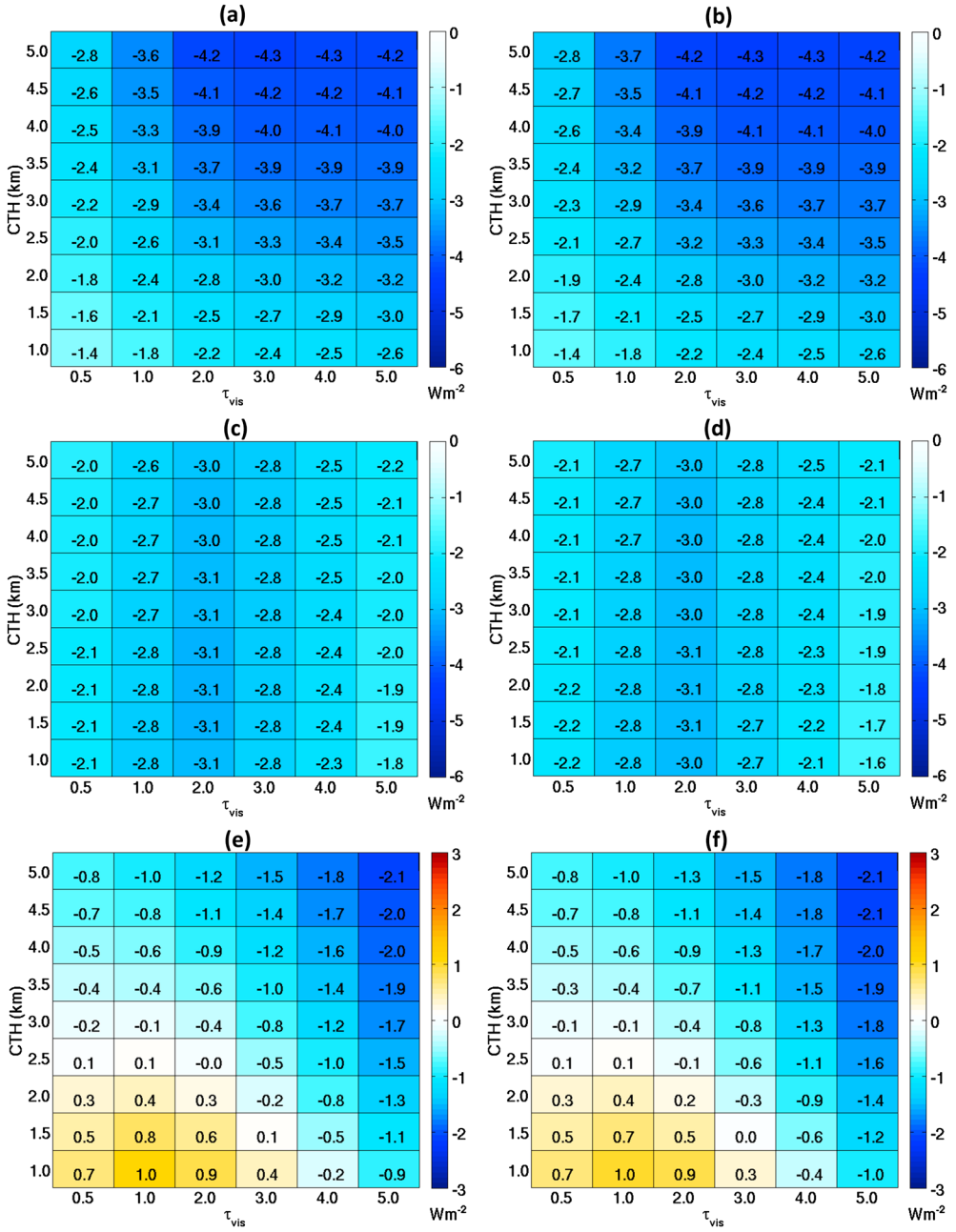

Figure 3. (a) The difference in TOA outgoing far-IR flux between Treatment 2 and Treatment 1 for the fine snow surface and varying cloud top heights and visible optical depths. (b) Same as Figure 3a except for the coarse snow surface. (c and d) Same as Figures 3a and 3b but instead showing the difference in surface net upward far-IR flux. The ratio of far IR to visible cloud extinction optical depth is ~1.12. (e) The difference between Figures 3a and 3c, i.e., the difference in net atmospheric emission in the far IR between Treatment 2 and Treatment 1 for the fine snow surface. (f) Same as Figure 3e but for the coarse snow surface. The cirrus effective size is assumed to be 25 μm.

Compared to Treatment 1 (Case 0 in Table 1), Treatment 2 (Cases 1 and 2 in Table 1) reduces monthly mean TOA upward far-IR flux by more than 0.84 Wm^{-2}. Compared to Case 3 (which includes scattering clouds but a blackbody surface), Treatment 2 (which includes both scattering clouds and nonblackbody surface) reduces monthly mean TOA upward far-IR flux by ~0.3 Wm^{-2} for fine snow and ~0.5 Wm^{-2} for coarse snow. Similar to Figure 4, the larger the cloud effective size is, the smaller the difference from Treatment 1. The change in surface net upward far-IR flux is similar in both magnitude and dependence with surface emissivity and cloud ice effective size. As a result, Treatment 2 reduces the monthly mean atmospheric

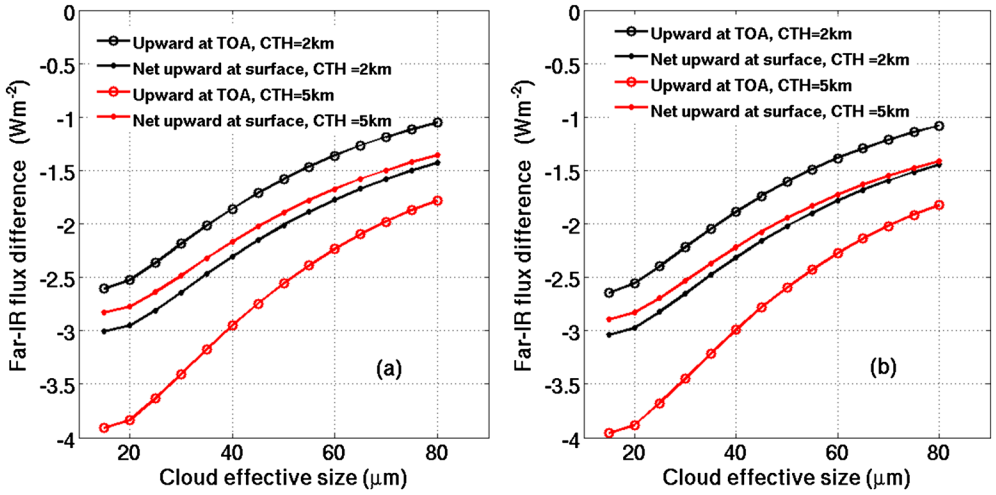

Figure 4. The sensitivity of far-IR flux difference between Treatment 2 and Treatment 1 with respect to the size of cirrus ice cloud particle. The visible cloud optical depth is assumed to be 1.0. (a) For the case of fine snow. (b) For the case of coarse snow.

far-IR net emission by 0.29 Wm^{-2} for both fine and coarse snow surfaces when cloud ice effective size is 25 μm. When cloud ice effective size is 50 μm, the net emission decrease is only 0.12 Wm^{-2}. When comparing the results of Case 3 with those of Cases 1 and 2, it is clear that even for such monthly averages of all-sky situations, the impacts of both factors (the snow spectral emissivity and ice cloud scattering) are discernible in both the TOA and surface radiation budgets. Moreover, the changes caused by the two factors have the same sign and comparable magnitudes.

In parallel to Table 1, we also examine the changes in TOA and surface radiation budgets in the middle IR bands as computed by the RRTM_LW (Figure S3 in the supporting information). This analysis shows that the only noticeable changes are associated with two window bands, and the magnitudes of total changes in the middle IR are much smaller than those in the far IR, which confirms our reasoning that the largest LW changes are expected in the far IR.

4. Conclusions and Discussions

We discuss the impact of including surface spectral emissivity and scattering by ice clouds on the surface and TOA far-IR radiation budgets of polar high-elevation regions. Sensitivity studies show that when scattering by ice clouds and spectral emissivity of snow surface are both taken into account, net upward far-IR flux at both the TOA and surface are reduced and the sign of change in atmospheric net far-IR emission depends on both cloud optical depth and cloud top height. Using one winter month of CloudSat and CALIPSO observations with ERA-Interim reanalysis, it is shown that the monthly mean decreases in both the TOA and surface net upward far-IR flux are ~0.72–1.47 Wm^{-2}. As a result, these changes lead to only an ~0.1–0.3 Wm^{-2} reduction of atmospheric net far-IR emission (or equivalent, an ~0.1–0.3 Wm^{-2} increase of atmospheric net far-IR absorption), smaller than the changes of far-IR flux at the TOA and surface.

Our sensitivity studies show that the impact of such treatments of surface emissivity and cloud longwave scattering on the wintertime local energy budget is nonnegligible and is sensitive to both the cloud particle size and the snow grain size. Our capabilities of measuring and modeling both cloud and snow grain sizes in the polar region are still limited. In addition, we still lack reliable measurements of far-IR surface spectral emissivity, making direct validation of modeled emissivity difficult. We hope that this study can raise enough attention in both modeling and observational communities to further look into these issues and improve the representations of far-IR radiative properties and processes in GCMs.

Acknowledgments
We thank M. Hori for providing the in situ measurements of snow middle IR spectral emissivity. We wish to thank two anonymous reviewers for their insightful comments, especially for pointing us to key literatures about in situ measurements of snow emissivity. We are also indebted to S. Warren for guiding us to an in situ study about the size of precipitating ice crystals in the Antarctic winter. X. L. Huang is thankful to Von P. Walden for stimulating discussions. The CloudSat data were obtained from the CloudSat Data Processing Center. The ECMWF-Interim data were obtained from http://data.ecmwf.int/data/. This research is supported by the NASA CLARREO project under grant NNX11AE68G awarded to the University of Michigan.

The Editor thanks two anonymous reviewers for their assistance in evaluating this paper.

References

Anisimov, O. A., D. G. Vaughan, T. V. Callaghan, C. Furgal, H. Marchant, T. D. Prowse, H. Vilhjálmsson, and J. E. Walsh (2007), Polar regions (Arctic and Antarctic), in *Climate Change 2007: Impacts, Adaptation and Vulnerability. Contribution of Working Group II to the Fourth Assessment Report of the Intergovernmental Panel on Climate Change*, edited by M. L. Parry et al., pp. 653–685, Cambridge Univ. Press, Cambridge, U. K.

Armour, K. C., I. Eisenman, E. Blanchard-Wrigglesworth, K. E. McCusker, and C. M. Bitz (2011), The reversibility of sea ice loss in a state-of-the-art climate model, *Geophys. Res. Lett.*, *38*, L16705, doi:10.1029/2011GL048739.
Baldridge, A. M., S. J. Hook, C. I. Grove, and G. Rivera (2009), The ASTER Spectral Library version 2.0, *Remote Sens. Environ.*, *113*, 711–715.
Berger, R. H. (1979), Snowpack optical properties in the infrared. U.S. Army Cold Regions Research and Engineering Laboratory CRREL Rep., *79*, 11 pp.
Chen, X. H., X. L. Huang, and X. Liu (2013), Non-negligible effects of cloud vertical overlapping assumptions on longwave spectral fingerprinting studies, *J. Geophys. Res. Atmos.*, *118*, 7309–7320, doi:10.1002/jgrd.50562.
Chou, M. D., K. T. Lee, S. C. Tsay, and Q. Fu (1999), Parameterization for cloud longwave scattering for use in atmospheric models, *J. Clim.*, *12*, 159–169.
Clough, S. A., M. W. Shephard, E. J. Mlawer, J. S. Delamere, M. J. Iacono, K. Cady-Pereira, S. Boukabara, and P. D. Brown (2005), Atmospheric radiative transfer modeling: A summary of the AER codes, *J. Quant. Spectrosc. Radiat. Transfer*, *91*, 233–244.
Costa, S. M. S., and K. P. Shine (2006), An estimate of the global impact of multiple scattering by clouds on outgoing long-wave radiation, *Q. J. R. Meteorol. Soc.*, *132*, 885–895.
Dee, D. P., et al. (2011), The ERA-Interim reanalysis: Configuration and performance of the data assimilation system, *Q. J. R. Meteorol. Soc.*, *137*, 553–597.
Deng, M., G. G. Mace, Z. Wang, and H. Okamoto (2010), Tropical Composition, Cloud and Climate Coupling Experiment validation for cirrus cloud profiling retrieval using CloudSat radar and CALIPSO lidar, *J. Geophys. Res.*, *115*, D00J15, doi:10.1029/2009JD013104.
Fu, Q., P. Yang, and W. B. Sun (1998), An accurate parameterization of the infrared radiative properties of cirrus clouds for climate models, *J. Clim.*, *11*, 2223–2237.
Hapke, B. (1993), *Theory of Reflectance and Emittance Spectroscopy*, 455 pp., Cambridge Univ. Press, New York.
Harries, J., B. Carli, R. Rizzi, C. Serio, M. Mlynczak, L. Palchetti, T. Maestri, H. Brindley, and G. Masiello (2008), The far-infrared Earth, *Rev. Geophys.*, *46*, RG4004, doi:10.1029/2007RG000233.
Holland, M. M., and C. M. Bitz (2003), Polar amplification of climate change in coupled models, *Clim. Dyn.*, *21*, 221–232.
Hori, M., et al. (2006), In-situ measured spectral directional emissivity of snow and ice in the 8–14 μm atmospheric window, *Remote Sens. Environ.*, *100*, 486–502.
Iacono, M. J., E. J. Mlawer, S. A. Clough, and J.-J. Morcrette (2000), Impact of an improved longwave radiation model, RRTM. On the energy budget and thermodynamic properties of the NCAR community mode, CCM3, *J. Geophys. Res.*, *105*, 14,873–14,890, doi:10.1029/2000JD900091.
Kay, J. E., M. M. Holland, C. M. Bitz, E. Blanchard-Wrigglesworth, A. Gettelman, A. Conley, and D. Bailey (2012), The influence of local feedbacks and northward heat transport on the equilibrium Arctic climate response to increased greenhouse gas forcing, *J. Clim.*, *25*(16), 5433–5450.
Li, J. (2002), Accounting for unresolved clouds in a 1D infrared radiative transfer model. Part I: Solution for radiative transfer, including cloud scattering and overlap, *J. Atmos. Sci.*, *59*, 3302–3320.
Masuda, K., T. Takashima, and Y. Takayama (1988), Emissivity of pure and sea waters for the model sea surface in the infrared window regions, *Remote Sens. Environ.*, *24*(2), 313–329, doi:10.1016/0034-4257(88)90032-6.
McClatchey, R. A., R. W. Fenn, J. E. A. Selby, F. E. Volz, J. S. Garing (1972), *Optical Properties of the Atmosphere*, 3rd ed., AFGRL-72-0497, 80 pp., Air Force Geophys. Lab., Bedford, Mass.
Mishchenko, M. I. (1994), Asymmetry parameters of the phase function for densely packed scattering grains, *J. Quant. Spectrosc. Radiat. Transfer*, *52*, 95–110.
Mishchenko, M. I., and A. Macke (1997), Asymmetry parameters for the phase function for isolated and densely packed spherical particles with multiple internal inclusions on the geometric optics limit, *J. Quant. Spectrosc. Radiat. Transfer*, *57*, 767–794.
Mlawer, E. J., S. J. Taubman, P. D. Brown, M. J. Iacono, and S. A. Clough (1997), Radiative transfer for inhomogeneous atmospheres: RRTM, a validated correlated-k model for the longwave, *J. Geophys. Res.*, *102*, 16,663–16,682, doi:10.1029/97JD00237.
Neely, R. R., and J. P. Thayer (2011), Raman lidar profiling of tropospheric water vapor over Kangerlussuaq, Greenland, *J. Atmos. Oceanic Tech.*, *28*, 1141–1148.
Oleson, K. W., et al. (2010), Technical description of version 4.0 of the Community Land Model (CLM). National Center for Atmospheric Research, *Tech. Rep. NCAR/TN–478+STR*, 266 pp., Boulder, Colo.
Screen, J. A., C. Deser, and I. Simmonds (2012), Local and remote controls on observed Arctic warming, *Geophys. Res. Lett.*, *39*, L10709, doi:10.1029/2012GL051598.
Shindell, D. (2007), Local and remote contributions to Arctic warming, *Geophys. Res. Lett.*, *34*, L14704, doi:10.1029/2007GL030221.
Stamnes, K., S. C. Tsay, W. Wiscombe, and K. Jayaweera (1988), Numerically stable algorithm for discrete-ordinate-method radiative transfer in multiple scattering and emitting layered media, *Appl. Optic*, *27*, 2502–2509.
von Salzen, K., et al. (2013), The Canadian Fourth Generation Atmospheric Global Climate Model (CanAM4). Part I: Representation of Physical Processes, *Atmos. Ocean*, *51*, 104–125.
Wald, A. E. (1994), Modeling thermal infrared reflectance spectra of frost and snow, *J. Geophys. Res.*, *99*, 24,241–24,250, doi:10.1029/94JB01560.
Walden, V. P., S. G. Warren, and E. Tuttle (2003), Atmospheric ice crystals over the Antarctic Plateau in winter, *J. Appl. Meteorol.*, *42*, 1391–1405.
Warren, S. G. (1982), Optical properties of snow, *Rev. Geophys. Space Phys.*, *20*, 67–89.
Warren, S. G., and R. E. Brandt (2008), Optical constants of ice from the ultraviolet to the microwave: A revised compilation, *J. Geophys. Res.*, *113*, D14220, doi:10.1029/2007JD009744.
Wiscombe, W. J., and S. G. Warren (1980), A model for the spectral albedo of snow, I: Pure snow, *J. Atmos. Sci.*, *37*, 2712–2733.
Wood, N. (2008), Level 2B Radar-Visible Optical Depth Cloud Water Content (2B-CWC-RVOD) Process Description Document, Version: 5.1, 26 pp., Colorado State Univ., Boulder, Colo.
Ye, H., E. J. Fetzer, D. H. Bromwich, E. F. Fishbein, E. T. Olsen, S. L. Granger, S.-Y. Lee, L. Chen, and B. H. Lambrigtsen (2007), Atmospheric total precipitable water from AIRS and ECMWF during Antarctic summer, *Geophys. Res. Lett.*, *34*, L19701, doi:10.1029/2006GL028547.